Dichotomy between tunneling and multiphoton ionization in atomic photoionization: Keldysh parameter γ versus scaled frequency Ω

Turker Topcu and Francis Robicheaux
Department of Physics, Auburn University, Auburn, Alabama 36849-5311, USA
(Received 27 September 2012; published 9 November 2012)

It is commonly accepted in the strong-laser physics community that the dynamical regime of atomic ionization is characterized by the Keldysh parameter γ. Two distinct cases, where $\gamma < 1$ and $\gamma > 1$, are associated with ionization mechanisms that are predominantly in the tunneling and in the multiphoton regimes, respectively. We perform fully three-dimensional quantum simulations for the ionization of the hydrogen atom by solving the time-dependent Schrödinger equation for a wide range of laser parameters encoded by the Keldysh parameter. We find that the meaning of the Keldysh parameter γ changes when the laser frequency ω is changed, and demonstrate that γ is useful in determining the dynamical ionization regime only when coupled with the scaled laser frequency Ω when a large range of laser frequencies and peak intensities are considered. The scaled frequency Ω relates the laser frequency ω to the classical Kepler frequency ω_K of the bound electron. Together with the Keldysh parameter, the pair (γ,Ω) refers to a more realistic picture of the dynamical ionization regime. We refer to final momentum distributions of the ionized electrons at several interesting points on the (γ,Ω) landscape in order to infer whether the tunneling or the multiphoton mechanism is dominant in these regions.

DOI: 10.1103/PhysRevA.86.053407 PACS number(s): 32.80.Rm, 05.45.Pq

I. INTRODUCTION

It has been ubiquitous in strong-laser physics that the dynamical regime of atomic ionization, whether it be tunneling or ionization through absorption of photons, is associated with the Keldysh parameter γ [1,2]. In strong lasers, the Coulomb field experienced by the atomic electron is depressed by the strong laser field. Depending on the peak field strength of the laser field, this depression can be substantial so as to result in a potential barrier oscillating at the laser frequency. Quantum mechanically, there is nonvanishing probability that the electron can tunnel through this barrier and escape into the continuum. The likelihood of ionization in this manner is quantified by the conditions in which the Keldysh parameter is less than unity, $\gamma < 1$. This is commonly referred to as the quasistatic limit, in which the depressed Coulomb barrier is essentially static as seen by the electron. When $\gamma > 1$, the atom ionizes by absorption of a number of photons and the electron escapes through either direct or indirect paths of ionization. However, $\gamma > 1$ does not necessarily mean that there is no tunneling contribution to the ionization; it implies that the tunnel ionization is least likely, and the electron is more likely to escape by absorbing photons.

Keldysh theory is strictly a theory of tunneling [1,2]. In Keldysh-like strong-field theories, the classical action is always complex regardless of γ, therefore its description is always contained within the tunneling picture. In other words, ionization through a classically allowed path does not occur in Keldysh-like theories. Therefore, the statement that $\gamma > 1$ corresponds to multiphoton ionization is not a statement made directly by the Keldysh theory, but rather is a deduction which incorporates conservation of energy with the prediction that $\gamma < 1$ refers to ionization dynamics governed predominantly by tunneling. It predicts the ionization rates when tunneling is most likely, and when there is ionization with $\gamma > 1$, we deduce that it must have followed an ionization path that is not tunneling, i.e., one characterized by absorption of photons. This is the step that incorporates the conservation of energy into the argument which ultimately decides that the ionization happens through photon absorption.

Several shortcomings of the Keldysh-like theories are evident from the approximations made to the S-matrix elements to allow for closed analytical expressions. For example, theories such as the strong-field approximation (SFA) involve no dynamics within the potential barrier, are not gauge invariant, and the result usually depends on the choice of the origin [3–6]. Less obvious shortcomings of the applicability of the Keldysh parameter as an index for assessing ionization regimes have also been demonstrated and it has been shown to be unsuitable to describe laser-induced ionization when a wide range of frequencies is considered. Even when $\gamma < 1$, the laser frequency can be so high as to allow for ultraintense fields, while keeping the Keldysh parameter small. In such instances, the $\gamma \to 0$ limit converges to the fully relativistic conditions, where the ponderomotive energy $U_p = F^2/4\omega^2$ becomes comparable to the rest energy of the electron [7] (we use atomic units throughout this paper). This invalidates the $\gamma \to 0$ limit as the static field limit in which ionization simply occurs through field ionization (tunneling or over the barrier). In another study [8], it was shown that high-energy plateau structures regularly attributed to tunneling in above-threshold ionization (ATI) and high-order harmonic generation (HHG) spectra can be seen in the multiphoton regime, provided that the photon energy is much smaller than the ponderomotive potential. This suggests that rescattering can occur even though the electron initially ends up in the continuum with substantial kinetic energy, as opposed to having no initial kinetic energy if it was to escape through tunneling.

The reasoning behind the Keldysh parameter is the following: In the standard Keldysh theory, the tunneling length is $L \sim I_p/F$, where I_p and F are the ionization potential and the peak electric-field strength, respectively. The velocity in the classically forbidden region, where the combined Coulomb and electric-field potential is larger than the total energy of

the electron, can be obtained using the WKB approximation to be roughly $v \sim \sqrt{2I_p}/2$. Then the time it takes for the electron to tunnel through the depressed Coulomb potential is essentially $\tau \sim L/v = \sqrt{2I_p}/F$. The ratio of this tunneling time to the laser period is a measure of how fast the barrier oscillates compared to the time it takes for the electron to tunnel ionize, i.e., $\omega\tau$, where ω is the laser frequency. This ratio is $\gamma = \omega\sqrt{2I_p}/F$ and is referred to as the Keldysh parameter. It tells how static the oscillating potential is as seen by the bound electron. The barrier is effectively static with regard to the time it takes the electron to tunnel ionize when $\gamma < 1$ (or $T > \tau$), and oscillating if $\gamma > 1$ (or $T < \tau$). The problem with exploiting the Keldysh parameter for a wide range of frequencies is immediately evident from this definition. Note that γ is linearly proportional to ω, whereas it is inversely proportional to F. Therefore, for a fixed laser wavelength, one can vary the laser intensity in ways such that any value for the Keldysh parameter can be attained. Conversely, fixing the field intensity, one can vary the wavelength to get any γ desired. This point of view does not necessarily take into account conservation of energy and the possibly relevant time scales other than the laser period, such as the classical orbital period of the electron. As a result, incorrect deductions can be made for ionization dynamics for certain sets of laser parameters. For example, assuming a fixed $\gamma \ll 1$, we can keep choosing smaller and smaller intensities for a laser pulse, which may push the photon energy well into the x-ray region. However, it would be unreasonable to expect that ionization by such a laser pulse would happen through tunneling.

Experiments such as the ones in Refs. [9,10] have suggested that the ratio of the laser frequency ω to the classical orbital frequency ω_K of the bound electron, i.e., ω/ω_K, could be just as relevant in deducing the dominant physical mechanisms as the laser frequency ω itself. This ratio is termed the scaled frequency and is given by $\Omega = \omega n^3$ for atoms. The reasoning behind this is evident if one considers that absorption of a photon by an atomic electron is most likely when the electron is near the nucleus. This happens once in every classical period $2\pi n^3$. When $\Omega < 1$, the effect of the field is similar to that of a static field and the field strength required for ionization scales like $F \sim 1/9n^4$. When $\Omega \to 1$, multiphoton transitions occur to higher n states, which are more easily ionized. In this regime, the ionization rate scales $\sim F^{2N}$, where N is the number of photons absorbed during ionization. $\Omega > n/2$ or $\omega > 1/2n^2$ is the single-photon ionization limit after which photoionization occurs through absorption of a single photon of higher frequency, and the field strength needed for ionization drops below $1/9n^4$.

For our purposes, it is more natural to express the Keldysh parameter in terms of the scaled parameters, Ω and $\mathcal{F} = Fn^4$, rather than ω and F. Scaling the field strength by $1/n^4$ and noting that $\omega = \Omega/n^3$, we can rewrite the Keldysh parameter in terms of the scaled frequency and the electric-field strength:

$$\gamma = \frac{\omega\sqrt{2I_p}}{F} \to \frac{(\Omega/n^3)\sqrt{1/n^2}}{\mathcal{F}/n^4} = \frac{\Omega}{\mathcal{F}}, \tag{1}$$

where the scaled frequency is $\Omega = \omega n^3 \sim \omega/\omega_K$. It is important to notice that after scaling the field strength and the frequency, the Keldysh parameter has no n dependence.

We perform two sets of calculations for the ionization of a hydrogen atom out of $1s$, $2s$, $8s$, and $16s$ states in laser fields: one for the ionization rate and one for the ionization probability for a large set of (γ,Ω) pairs. We map out a landscape in (γ,Ω) space, which shows regions bearing characteristics that can be attributed to either tunneling or multiphoton features. Then, calculating final momentum distributions of the ionized electrons at a select few points on the (γ,Ω) map for large and small γ, we investigate whether tunneling or multiphoton ionization is dominant in these regions. Unless explicitly stated otherwise, we use atomic units throughout this paper.

II. NUMERICAL SIMULATIONS

In our simulations, we drive the atom using a continuous-wave (cw) laser field in the rate calculations and a laser pulse in the probability calculations. All of our simulations are based on *ab initio* solutions of the three-dimensional time-dependent Schrödinger equation in the length gauge. We represent the total wave function on an (l,r) grid with a square-root mesh in the r direction. We use the lowest-order split operator technique for the time propagation of the Schrödinger equation, where each split piece is propagated using an $O(\delta t^3)$ implicit scheme. This is an exactly unitary propagator and enables us to use larger time steps during the time propagation compared to those needed for an explicit scheme. We use a mask function, which runs from 2/3 of the distance from the origin to the box edge, to remove the ionized part of the wave function in order to evade spurious reflections from the box edge. A detailed account of the $O(\delta t^3)$ implicit method and the split operator technique employed in this work can be seen in Ref. [11]. Below we only discuss the differences in our simulations for the ionization rates and probabilities. The number of the (γ,Ω) pairs we include in our simulations is 12 000, which is achieved by massive parallelization over all (γ,Ω) pairs.

We use a time-dependent method inspired by the time-dependent perturbation theory for our rate calculations. We split the total Hamiltonian of the system into two pieces, such that $H(r,l,t) = H_A(r,l) + H_L(r,t) - E_0$, where H_A is the atomic Hamiltonian and H_L is the Hamiltonian describing the interaction of the atom with the laser field in the length gauge:

$$H_A(r,l) = -\frac{1}{2}\frac{d^2}{dr^2} - \frac{1}{r} + \frac{l(l+1)}{2r^2}, \tag{2}$$

$$H_L(r,t) = F(t)z\cos(\omega t). \tag{3}$$

We subtract the energy of the initial state E_0 from the Hamiltonian, and express the total wave function as a superposition of the initial eigenstate of H_A and the time-dependent correction, $\psi(r,l,t) = \psi_0(r,l) + \psi_1(r,l,t)$, to write the time-dependent Schrödinger equation as

$$\left[i\frac{\partial}{\partial t} - H(r,l,t)\right]\psi_1(r,l,t) = H_L\psi_0, \tag{4}$$

with $H_L(r,t)\psi_0(r,l)$ acting as a source term. Dividing up the wave function into ψ_0 and $\psi_1(t)$ in this manner is particularly useful when the amplitude in $\psi_1(t)$ is much smaller than the amplitude in ψ_0. In this case, solving for $\psi_1(t)$ by itself substantially reduces the round-off errors when it comes to

extracting $\psi_1(t)$ from the total wave function. Given that $\psi(t) = \psi_0 + \psi_1(t)$, and that ψ_0 is an eigenstate of H_A, Eq. (4) is exact and allows for atomic processes of all orders, such as absorption of multiple photons, as well as single-photon processes and tunneling. The wave function $\psi_1(t)$ is zero everywhere before the laser pulse is turned on and it encodes the time-dependent corrections to the initial wave function ψ_0. As the laser field is turned on, amplitude pours out of the initial state ψ_0 into ψ_1 at a rate defined by the instantaneous field strength. The time-dependent envelope for turning on the cw laser field is

$$F(t) = \begin{cases} F_0 \exp[-(t/\Delta t)^4], & t < 0 \\ F_0, & t \geqslant 0, \end{cases} \tag{5}$$

where we take Δt to be ten laser periods. We found that faster turn-on times result in ringing in the ionization flux, which starts to increase the propagation time required for the ionization rate to settle down at a steady state. On the other hand, slower turn-on rates also result in higher computational overhead since they prolong the total propagation time of Eq. (4).

After the peak of the laser envelope is reached ($t \geqslant 0$), we wait for the time-dependent ionization flux $J_R(t)$ to settle down at a steady state, which we then interpret as the ionization rate. The time-dependent flux $J_R(t)$ through a spherical surface far away from the origin is

$$J_R(t) = -\mathrm{Re}\left[i \sum_l \psi_1^*(R,l,t) \left. \frac{\partial \psi_1(r,l,t)}{\partial r} \right|_{r=R} \right]. \tag{6}$$

Here, R is the radius of the spherical surface through which we evaluate the flux. It is also the distance from the origin beyond which the mask function becomes effective.

In a second set of calculations, we explore the ionization probabilities in the (γ,Ω) parameter space. In contrast with the ionization rate simulations described above, this would yield results which can be interpreted as actual ionization cross sections from a finite width laser pulse. This way we can more directly associate structures seen in the (γ,Ω) landscape with different ionization mechanisms and furthermore investigate momentum distribution of the escaping part of the wave function. To calculate the ionization probabilities, we solve the time-dependent Schrödinger equation:

$$\left[i \frac{\partial}{\partial t} - H(r,l,t) \right] \psi(r,l,t) = 0, \tag{7}$$

with the initial wave function being a bound state of hydrogen with $l = 0$, i.e., $1s$, $4s$, and $8s$. Note that the operator acting onto $\psi(r,l,t)$ on the left-hand side is the same operator as in Eq. (4). However, in this case, a laser pulse is used rather than a cw laser field, and the pulse envelope is Gaussian with a width of 160 classical periods at FWHM. We evaluate the ionization probability as the norm of the wave function, which is absorbed by the mask starting from 2/3 of the distance from the box origin, with the initial wave function normalized to unity. In contrast to the rate calculations, the amount of ionization probability depends on the width of the laser pulse used.

In all of our calculations, we regularly perform convergence checks on several relevant numerical parameters, such as the number of grid points and angular momenta as well as the size of the time steps taken during the propagation of Eqs. (4) and (7). Since there are two inherent time scales involved in the problem, i.e., the Rydberg period τ_R of the electron and the laser period $2\pi/\omega$, we pay special attention to our choice of the time step to make sure that we have enough points in time within the smallest time scale for a given (γ,Ω) pair.

In choosing the number of grid points N for a box of size R using the square-root mesh in the r direction, we make sure that $\max(k\delta r) < 1$ everywhere inside the box. Specifically, we monitor $k\delta r$ where the mask function starts at the box edge $[\max(k\delta r_R)]$. Given that we use a square-root mesh with $r_j = j^2 R/N^2$ $(0 \leqslant j < N)$, and a mask function starting from 1/3 of the way from the box edge, we deduce that

$$\max(k\delta r_R) = \frac{2R}{N}[2\Omega_{\max}/n^3]^{1/2}, \tag{8}$$

where $k = (2E)^{1/2}$ and $\Omega_{\max}$ is the maximum Ω we consider in the (γ,Ω) space. The grid spacing $\delta r_R = 2R/N$ is the largest grid spacing at the end of the radial box. We find that our results for the rate calculations are reasonably converged when $\max(k\delta r_R) \sim 0.76$ for $n = 1$, $\sim$0.36 for $n = 4$, and $\sim$0.32 for $n = 8$. In the probability calculations, we had $\max(k\delta r_R)$ values smaller than these by a factor of 4 because we only go up to $\Omega = 4$ in the probability calculations, whereas the maximum Ω is 64 in the rate calculations. Note that the effective $k\delta r$ in these calculations is smaller than the one given by Eq. (8) because δr_R is the grid spacing at the box edge, where the ionized part of the wave function is already absorbed and removed from the box.

III. RESULTS AND DISCUSSION

A. Ionization rate

Figure 1 shows the steady flux of ionizing electrons, which we interpret as the ionization rate Γ, from initial states of $1s$, $4s$, $8s$, and $16s$ for a hydrogen atom. The scaled frequency Ω ranges from 0.05 to 64 and is plotted in $\log_2$ scale to display such a wide range of frequencies in a single plot. The vertical axes are the Keldysh parameter γ, which ranges from 0.1 to 2 a.u. and is plotted in linear scale. The ionization rates Γ are plotted in $\log_{10}$ scale and the contours decrease from yellow (bright) to blue (darker). For a fixed Ω, the ionization rate ultimately increases as γ decreases because γ is inversely proportional to the field strength at fixed Ω. This is expected since no matter what the frequency is, there is a high enough field strength which will result in ionization. For the lowest Ω value in Fig. 1, F varies from 1.3×10^7 to 6.4×10^7 V/cm as γ varies from 2 to 0.1, which corresponds to intensities of $\sim 9 \times 10^{15}$ and $\sim 4 \times 10^{14}$ W/cm^2. On the other hand, for the highest Ω, the electric-field strength varies between 32 and 640 a.u. as γ varies from top to bottom, which corresponds to ultrahigh intensities of $\sim 10^{18}$ and $\sim 2 \times 10^{19}$ W/cm^2, respectively. These four intensities correspond to the four limiting cases situated at the four corners of each (Ω,γ) map.

Photon energies in eV corresponding to the Ω values are also indicated on the upper horizontal axis for reference. Note that even the minimum of these intensities is fairly large for a hydrogen atom. This stems from our choice for the ranges of Ω and γ in Fig. 1, which is motivated by the desire to straddle $\gamma = 1$ in an Ω range that runs from $\Omega \ll 1$ to $\Omega \gg 1$. In reality,

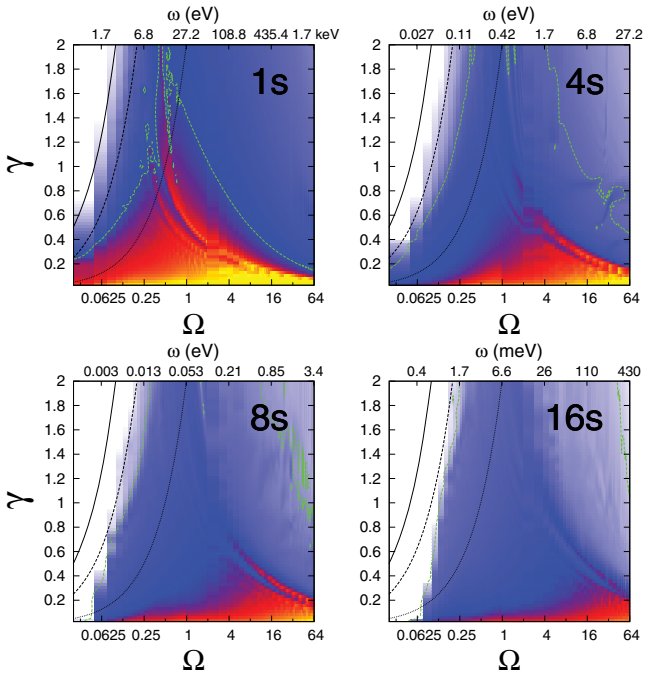

FIG. 1. (Color online) Ionization rate Γ vs the Keldysh parameter γ and the scaled frequency Ω for $n = 1, 4, 8$, and 16 with the atomic wave packet launched as an s wave. Along the solid, dashed, and dotted black lines, $F = 0.05$, 0.1, and 0.5 a.u. from left to right, where F is the peak electric-field strength. The Ω axes are in $\log_2$ scale, whereas the γ axes are in linear scale. The ionization rates Γ are plotted in $\log_{10}$ scale with the brightest yellow being 2 a.u. and the faintest blue being −4.5 a.u. The dashed green lines mark the classical orbital frequency $1/(2\pi n^3)$ for each initial state.

for most of the (Ω,γ) pairs in Fig. 1, complete ionization occurs for a laser pulse that spans even a few classical periods of the electron. The important thing to remember here is that Fig. 1 is a map for the ionization *rate*.

The fact that ionization would saturate immediately for most of the maps in Fig. 1 is evident from the green contours. The regions enclosed by these contours are where the ionization rates are larger than the classical frequency $1/(2\pi n^3)$, i.e., where the ionization happens in less than a classical orbital period of the electron. In this case, rate as a concept ceases to be meaningful, and any structure within these interior regions of the green curves tells little about the dynamics leading to ionization since the ionization probability will very quickly saturate.

One striking feature in these maps is the ridge structure, which can be seen for $1s$ most clearly. Although they do not appear to be vertically straight due to the $\log_2$ scaling of the Ω axis, each of these ridges are at a fixed Ω value. Also note that there is more than one ridge in these figures. These correspond to the Ω that are the 1-, 2-, . . . , N-photon ionization thresholds and can be written as $\Omega_N = \omega_N/\omega_K = n/(2N)$. Here ω_N is the laser frequency needed for N-photon ionization. The most prominent ridges are those for $N = 1$ (single-photon ionization), and the smaller subsequent ridges to its left are the ones that correspond to multiphoton ionization with the absorption of two or more photons. In this multiphoton region, $\Omega < n/2$, and the ridges gradually disappear as $\Omega \to 0$, when the oscillation of the laser field becomes much slower than the classical orbital motion of the electron. In this case, the depressed Coulomb potential is essentially static with regard to the tunneling time of the electron, and ionization mainly occurs through tunneling for all γ. For $\Omega < n/2$ with $\gamma > 0.5$, the ionization rate drops drastically, even well before $\gamma = 1$ is reached.

To the right side of the single-photon ionization ridge, the ionization rate drops with increasing photon energy for a fixed γ. In this region of high scaled frequency, ionization is suppressed and higher and higher photon intensities are required to maintain a given rate of ionization if Ω is increased. This suppression of ionization has been observed in experiments for microwave ionization out of high-Rydberg states [12,13]. It can be understood considering that the higher the Ω, the smaller fraction of its orbit the electron will spend near the nucleus, where it is most likely to absorb a photon, thus rendering the electron less able to absorb photons. An alternative way to think about this is that absorption of a photon with a larger Ω would result in a larger energy change. The bigger the energy change in the final wave function, the smaller the region of space is where the initial and final wave functions have similar momenta $k(r)$. The absorption of a single photon is sufficient for ionization in this region. For instance, at 1.7 keV for $1s$, γ needs to be less than 0.3 for $\Omega > 16$ in order to maintain the same ionization rate for $\Omega \sim 4$. Clearly, we cannot say that ionization at these high Ω occurs through tunneling, and the statement that $\gamma < 1$ refers to tunneling is misleading.

On top of the (γ,Ω) maps in Fig. 1, we plot lines along which the peak electric-field strength is a constant. The solid, dashed, and dotted lines correspond to $F = 0.05$, 0.1, and 0.5 a.u., respectively, and such slices in Fig. 1 can be taken to extract the energy spectrum at a fixed intensity. In the left column of Fig. 2, we take the spectroscopic point of view for photoionization and depict ionization rates as a function of Ω for three individual field strengths for the initial states of $1s$, $4s$, and $8s$ corresponding to the constant F slices seen in the (γ,Ω) maps of Fig. 1. The ionization rate which equals the classical frequency $1/(2\pi n^3)$ is indicated for each initial state by the horizontal dashed lines in the left column of Fig. 2 (corresponding to green contours in Fig. 1). Portions of the curves that lie above the green lines in Fig. 1 correspond to cases in which ionization occurs in less than a classical period and should not be interpreted as ionization rates. The rates are plotted in $\log_{10}$ scale as in Fig. 1, although the Ω axis is now in linear scale. $F = 0.5$, 0.1, and 0.05 a.u., from top to bottom in each panel on the left, and, as expected, the overall magnitudes of the ionization rates drop as the peak field strength decreases. This is due to the well-known power-law dependence of the rate on the intensity for an N-photon absorption process, $\Gamma \sim F^{2N}$ (see [2] and references therein). Although the intensities seen in this column are somewhat high for hydrogen, ionization with two distinct characteristics can be easily identified in the low- and the high-frequency regions. In the low-Ω part of the spectra, the rates drop much faster with the decreasing intensity when compared with the higher-frequency region. This is a manifestation of the Ω-independent decay in the tunneling regime, where the decay rate decreases exponentially with the inverse of the field strength, i.e., $\Gamma \sim \exp[-2(2I_p)^{3/2}/(3F)]$ in the static field limit [2]. On the other hand, before the sharp

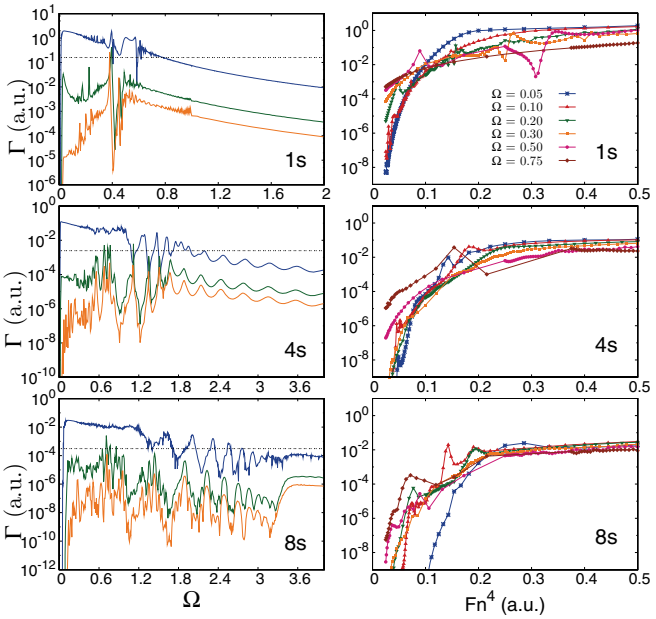

FIG. 2. (Color online) Left column: Ionization rates Γ as a function of the scaled frequency Ω out of $n = 1s$, $4s$, and $8s$ states of the hydrogen for three different peak field strengths: $F = 0.05$, 0.1, and 0.5 a.u. from top to bottom. These correspond to intensities of 1.8×10^{17}, 3.6×10^{15}, and 1.8×10^{15} W/cm^2. The Γ axes are in $\log_{10}$ scale. The dashed lines mark the classical frequency of the electron in its initial state for each panel. Right column: Γ as a function of the scaled peak electric-field strength Fn^4 for several Ω for ionization out of the same states. Again, the Γ axes are plotted in $\log_{10}$ scale.

drop in the rate is reached for small Ω, there is a relatively flat region which shows little dependence on the scaled frequency. This Ω-independent part of the spectra is the tunneling region, in which Γ obeys the exponential decay of the ionization rate.

In contrast, the rate displays structures in the higher-frequency region, which correspond to the multiphoton resonance structure of the atom. The Rydberg-sequence structure of the multiphoton peaks marks the indirect paths of excitation followed by multiphoton ionization from an excited state. The positions of these peaks experience ac stark shifts from the laser field, and the position of Ω_1 is closest to $n/2$ for the lowest F. This regime persists until the higher Ω region is reached beyond the single-photon ionization limits $\Omega_1 = 0.5$, 2, and 4 for $n = 1$, 4, and 8. The ionization in this region is mainly described by Fermi's golden rule and the drop in the rate in this case is due to the power-law dependence of Γ on the intensity. An important caveat here is that when we refer to multiphoton ionization, we are not making any distinction between direct and indirect paths of ionization through absorption of many photons.

After the multiphoton structure is diminished beyond the single-photon ionization limit, the ionization is again suppressed, as discussed in [12,13] for Rydberg atoms in microwaves. This suppression is argued to be a quantum-mechanical interference effect, and the field needed for ionization tends to be n independent. Such a trend can also be seen in the left column in Fig. 2; as the region of high Ω is penetrated beyond Ω_1, the order of magnitude rates qualitatively start agreeing for $n = 4$ and 8.

Assuming the strong-field physics point of view, the right-hand column of Fig. 2 shows the ionization rates out of the same set of initial states of the hydrogen as a function of the scaled electric-field strength Fn^4 for various scaled frequencies. These plots correspond to constant vertical Ω slices in Fig. 1, and they are plotted as a function of the field strength Ω/γ rather than the Keldysh parameter. Notice that for the low values of Ω, there is a flat plateau region after $Fn^4 \gtrsim 0.2$, suggesting that the ionization rate drops like $1/n^4$ in this region. This is a signature of the static field tunnel ionization regime, and the distinction between ionization rates for different Ω disappears in this region. This is especially so for the higher n. The higher the principal quantum number, the more independent is the rate from the scaled frequency Ω. The rate at the single-photon ionization limit is only plotted for $1s$ ($\Omega_1 = 0.5$), and higher-order photoionization peaks appear at the low-field end of the $4s$ and the $8s$ plots. For the lowest fields in these figures, Γ for the higher frequencies drops much faster than the lower ones, which is a behavior more pronounced for the higher n states. This can again be understood considering that at low Ω, the rates decay according to the exponential law $\Gamma \sim \exp[-2(2I_p)^{3/2}/(3F)]$. Recalling that the field scales like $\sim 1/n^4$, and the ionization potential like $\sim 1/n^2$, the exponent would increase as $\sim n$ when plotted against the field strength, resulting in the diminishing of the ionization rate.

B. Ionization probability

Figure 3 shows the ionization probabilities out of $1s$, $4s$, and $8s$ states for hydrogen in (γ,Ω) space, where γ varies between 0 and 64, and Ω varies between 0.025 and 4. In contrast to the rate calculations, the probability calculations are performed using a finite-duration laser pulse with a width of 160 Ry periods at FWHM. This corresponds to a pulse width of 80 fs for $1s$, ~1.5 ps for $4s$, and ~12 ps for the $8s$ state. The contours are color coded such that the bright yellow regions indicate saturation of the ionization probability, i.e., complete ionization. An important difference to keep in mind when relating Fig. 3 to Fig. 1 is that the γ and Ω axes span different ranges in these figures. The γ axis goes up to 2 in Fig. 1 and up to 64 in Fig. 3, whereas the Ω axis goes up to 64 in Fig. 1 and up to 4 in Fig. 3. Also the Ω axis is in linear scale in Fig. 3, which is why the curved ridges seen in Fig. 1 are replaced by the straight peaks occurring at fixed values of Ω in Fig. 3. Regions with $\gamma < 2$ in Fig. 3 are essentially all saturated for the pulse width used for these simulations as needed to go up in γ as high as ~60, to see the larger picture. For a shorter pulse than ours, the extent of the saturated regions for all Ω would recede to lower γ, and eventually ranges seen in Fig. 1 are recovered when the pulse duration is shortened to a couple of classical periods. In that case, however, the pulse duration is at the attosecond scale, and even some of the high Ω would then be considered in the field-ionization regime.

As in Fig. 1, the multiphoton ionization peaks are unmistakable and they extend to high values of the Keldysh parameter due to the long pulse duration. The single-photon ionization frequency Ω_1 is again situated at $n/2$, and it is here that the ionization probability is the largest for the widest range of γ. This would be expected from Fig. 1; however, one feature that was not clear from Fig. 1 is that the broad

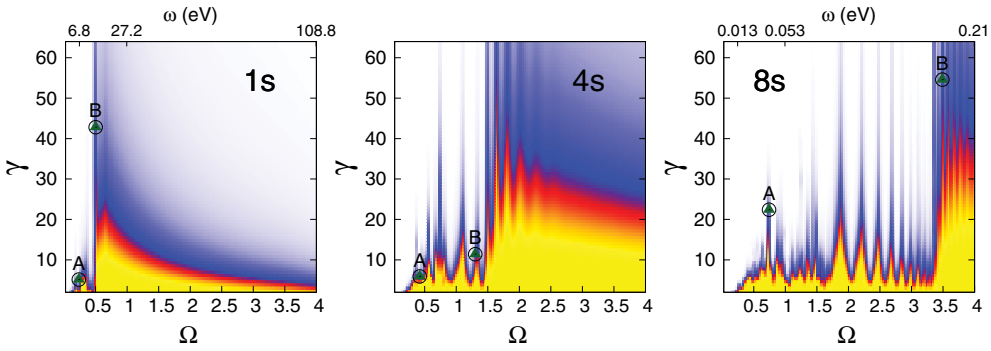

FIG. 3. (Color online) Quantum ionization probabilities for ionization out of $1s$, $4s$, and $8s$ states of the hydrogen for a laser pulse with a width of 160 Ry periods at FWHM. Both Ω and γ axes are in linear scale and the ionization probabilities are in $\log_{10}$ scale. The yellow regions indicate complete ionization, and the multiphoton ionization peaks as well as the suppression at high scaled frequencies are clearly visible. Momentum distributions for the points marked as A and B in each panel are seen in Fig. 4.

region centered at Ω_1 is split into subpeaks for $n = 4$ and 8. We believe that these peaks are due to the energy splitting between the degenerate l states inside the n manifolds, and the number of these peaks matching almost one unit of Ω supports this suspicion. As in the rate calculations, multiphoton peaks lead to the single-photon ionization limit and mark regions of ionization involving multiphoton processes following both direct and indirect paths. Many of these paths result in ionization following an excitation to an excited state, which is evident from the Rydberg-series-like structure leading up to Ω_1. However, regions in which the ionization happens through a direct multiphoton transition to the continuum, or via an assisted indirect process, are not distinguishable in these (γ,Ω) maps. The slow-decaying tail of the ionization probability beyond the single ionization limit Ω_1 is again indicative of the suppression of ionization at high scaled frequencies due to the stabilization seeded by quantum interferences, as reported in Refs. [12,13].

The entire (γ,Ω) region seen in Fig. 3 is for $\gamma \gg 1$. This is a result of the long laser pulse we use to keep the laser duration reasonably long for the entire Ω range we considered. Here reasonably long means longer than what would be considered an attosecond pulse duration. For laser pulses shorter than the one we used, ionization probabilities would be lower and they would saturate at smaller values of γ than seen in Fig. 3. From the common Keldysh parameter point of view, this is to say that everything seen in Fig. 3 is in the multiphoton regime, and no tunneling takes part in constructing the landscape depicted in Fig. 3. Although Fig. 3 does not distinguish tunneling regions from the multiphoton regions in any way beyond the Keldysh criteria, one may be inclined to assume the Keldysh viewpoint due to the multiphoton peaks that appear for $\Omega < n/2$ and extend high up in γ. In order to assess the extent of the multiphoton character in these regions, and to determine if any tunneling contributes to the overall ionization, we look at the momentum distributions of the ionized part of the wave function at various points on the (γ,Ω) landscape seen in Fig. 3.

IV. MOMENTUM DISTRIBUTIONS

In order to evaluate the momentum distribution of the ionized electrons, we follow the same procedure outlined in Ref. [9]. For the sake of completeness, here we briefly describe the method. In the rate and probability calculations we reported so far, the ionized part of the wave function is removed from the box every time step during the propagation of Eq. (7), in order to prevent unphysical reflections from the radial box edge. This is done by multiplying the wave function with a mask function $m(r)$, which is unity up to a distance of 2/3 of the box size from the origin, and decreases quadratically with distance until the box edge from there on. We retrieve the removed part of the wave function by evaluating

$$\Delta\psi_l(r,t') = [1 - m(r)]\psi_l(r,t') \tag{9}$$

at every time step, and Fourier transform it to get the momentum-space wave function $\Delta\phi(p_\rho,p_z,t')$,

$$\Delta\phi(p_\rho,p_z,t') = 2\sum_l (-i)^l\, Y_{l,m}(\theta,\varphi) \times \int_0^\infty j_l(pr)\Delta\psi_l(r,t')r^2dr. \tag{10}$$

Here the momentum $p = (p_\rho^2 + p_z^2)^{1/2}$ is in cylindrical coordinates and $j_l(pr)$ are the spherical Bessel functions. We then time propagate $\Delta\phi(p_\rho,p_z,t')$ to a later final time t using the classical action S,

$$\Delta\phi(p_\rho,p_z,t) = \Delta\phi(p_\rho,p_{1z},t')e^{-iS}. \tag{11}$$

This is numerically exact under the assumption that the dynamics of the electron in the laser field after ionization is treated classically. For the time-dependent laser field $F(t)$, action S is calculated numerically by integrating p_z^2 along the laser polarization direction,

$$S = \frac{1}{2}p_\rho^2(t-t') + \frac{1}{2}\int_{t'}^{t} p_z^2(t'')dt'', \tag{12}$$

$$p_z(t'') = p_{1z} - \int_{t'}^{t''} F(t)dt, \tag{13}$$

$$p_{1z} = p_z + \int_{t'}^{t} F(t'')dt''. \tag{14}$$

We are assuming that the ionized electron is freely propagating in the classical laser field in the absence of the Coulomb field of its parent ion.

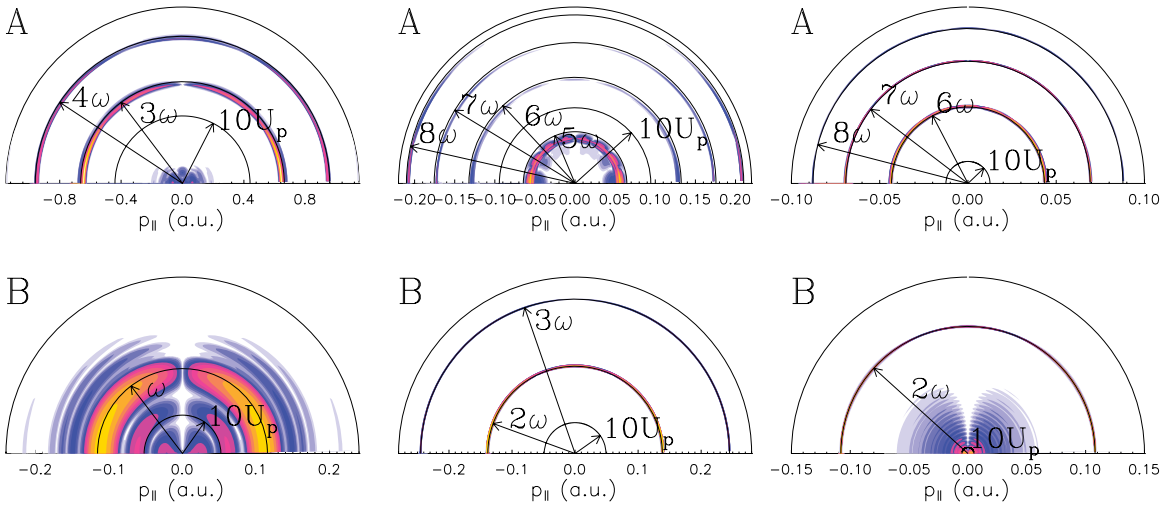

FIG. 4. (Color online) Momentum maps for the $\gamma > 1$ region for selected points from the ionization probability landscapes of Fig. 3. The momentum distributions have only the momentum component parallel to the laser polarization marked as the $p_{||}$ axis and the perpendicular component is implied from the cylindrical symmetry of the problem. Dashed semicircles marked as ω, 2ω, 3ω, etc. are the momentum rings corresponding to the multiphoton ionization from each initial state for a given (γ,Ω) pair. Similarly, the momentum rings corresponding to the $10U_p$ limit are also marked. The probabilities are plotted in logarithmic scale of base e to bring out both multiphoton and tunneling features on the same plot.

We picked two points in each panel of Fig. 3 to point out features that are commonly attributed to either multiphoton or tunneling ionization in the momentum distributions in the large γ region. We label these points as A and B in Fig. 3, and the corresponding momentum distributions are seen in Fig. 4, with the horizontal axis being the momentum component parallel to the laser polarization. The three columns in Fig. 4 correspond to the three panels in Fig. 3 for $1s$, $4s$, and $8s$, respectively. The momentum distributions are in logarithmic scale with the contours decreasing in factors of e in all cases. In all of these momentum distributions, momenta corresponding to three different energies are marked with dashed semicircles: (a) energy of the electron when it escapes by absorbing the necessary number of photons from its initial state (labeled as ω, 2ω, 3ω, etc. rings) and (b) the $10U_p$ limit. Classically, the electron can acquire kinetic energy up to $2U_p$ in the laser field, which is the maximum energy it can attain if it tunnels into the continuum and then escapes via the laser field alone without rescattering with its parent ion. The electron can acquire additional energy beyond this limit if rescattering occurs, and typically there is a relatively flat plateau region in the energy distribution of the photoelectrons following $2U_p$, which cuts off around $\sim 10U_p$ [14,15].

There are a few common physical characteristics seen in the momentum maps of Fig. 4. First, ionization by photon absorption is manifested as rings with radii $p \simeq \sqrt{2(N\omega - I_p)}$, where N is equal to or greater than the minimum number of necessary photons required for ionization. These rings are centered at $p = 0$ a.u., suggesting that the ionization is directly from the initial state and the electron escapes without rescattering with the ion. The centers of these rings can be shifted by as much as $\sim 10U_p$ when rescattering occurs [16]. Another common feature, seen in Fig. 4, is that the distributions are symmetric with respect to the reflection about the $p_{||} = 0$ plane because the laser pulses at the points marked as A and B in Fig. 3 are many-cycle pulses. Since the ejected electron escapes essentially along the polarization axis of the laser, the multiphoton rings and the tunneling momentum distributions are more intense close to the polarization direction. The ionization yield drops when the observation angle is increased off the laser polarization axis, which is clear from the momentum distributions in Fig. 4. Since we start from s states of the hydrogen atom in all of our calculations, absorption of an even number of photons results in an even ℓ, whereas absorption of an odd number of photons results in an odd ℓ of the ejected electron. This information is encoded in the multiphoton rings of Fig. 4 as nodes along the momentum rings. For example, the momentum rings due to electrons ejected by absorption of an odd number of photons have nodes in the direction perpendicular to the polarization axis, whereas rings resulting from absorption of an even number of photons have maxima.

All of the momentum distributions seen in Fig. 4 are dominated by multiphoton ionization rings. For instance, in the first column of Fig. 4, $\Omega = 0.24$ for point A, and the atom needs to absorb at least three photons to ionize from the $1s$ state. The corresponding three-photon absorption ring is stronger than the four-photon absorption ring, which is not surprising since the photoabsorption rate drops as $\sim F^{2N}$ for a given F, where N is the number of the absorbed photons. Similar observations can be made for the $4s$ and the $8s$ columns of Fig. 4. Since all of the points in Fig. 3 have γ much larger than one, the appearance of the photoabsorption rings in Fig. 4 is not surprising, and it is in agreement with the statement that $\gamma > 1$ corresponds to multiphoton ionization. However, there are also points with a substantial amount of amplitude at low momenta despite their large γ. For instance, the points marked as B in the $1s$ and the $8s$ panels of Fig. 3 display low-momentum components in their momentum distributions in Fig. 4. Although low-momentum distributions are usually

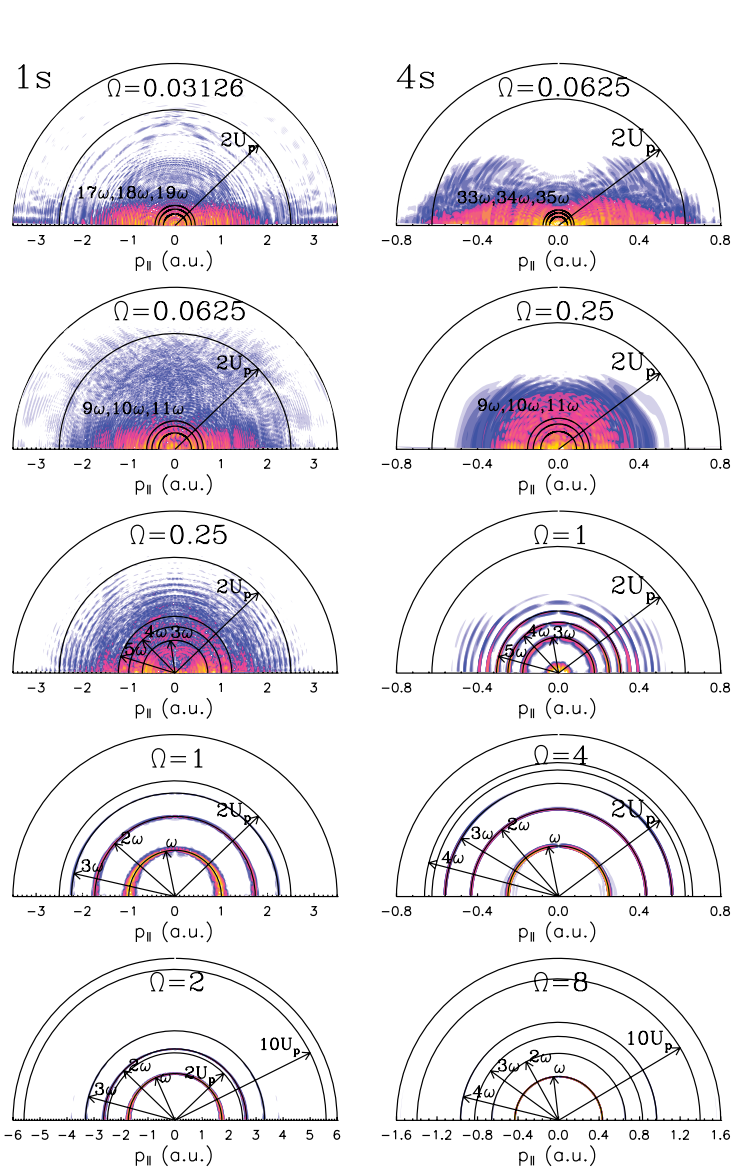

FIG. 5. (Color online) Momentum distributions for the low Keldysh parameter $\gamma = 0.4$ for ionization out of the $1s$ and the $4s$ states. In each column, Ω is varied from low to high going from top to bottom, while γ is kept fixed. The minimum number of photons Ω_1/Ω is also shown to the right of each row. Semicircles mark the photoabsorption momentum rings (labeled as ω, 2ω, etc.), as well as the $2U_p$ and the $10U_p$ limits.

recognized as electrons which escape through tunneling, they are not necessarily a definite signature of tunnel ionization. In other words, electrons can be ejected with low momenta even though their escape cannot be attributed to tunneling. For example, if the atom is driven exactly on resonance with the single-photon ionization threshold, then the ejected electrons have no kinetic energy upon escape. Depending on the width of the laser pulse in energy, these electrons would appear as low-momentum electrons in the momentum distribution with a certain spread around $p = 0$. In fact, both of the points labeled as B in the $1s$ and the $8s$ panels of Fig. 3 are just below their respective single-photon ionization limits in Ω. On the other hand, both of these points manifest a p-wave character in their momentum distributions at low momenta in Fig. 4. Combined with the fact that all of our calculations start with an s state and both points lie just below their single-photon ionization thresholds, it is clear that the low-momentum distributions seen at these points are due to electrons ejected by the absorption of a single photon in the spectral tails of the laser pulse and cannot be attributed to tunneling.

We have investigated many other points than those whose momentum distributions are seen in Fig. 4 and we did not encounter any cases where tunneling plays a role. This is in complete accord with the argument based on the value of the Keldysh parameter that $\gamma > 1$ implies multiphoton ionization. In the opposite case, where $\gamma < 1$, the same argument predicts that tunneling dominates the ionization dynamics. To find a case contradicting this, we look at momentum distributions for ionization out of the $1s$ and the $4s$ states at a fixed Keldysh parameter $\gamma = 0.4$, while scanning the frequency from low Ω to high Ω. The momentum distributions for five values of Ω varying in factors of 2 are seen in Fig. 5. The first column is for ionization out of the $1s$ state and the second column is for ionization from $4s$. To the right of the columns, we give the minimum number of photons Ω_1/Ω that would be necessary for photoionization for the corresponding values of Ω in each row. For example, $\Omega = 0.25$ for $1s$ and $\Omega = 1$ for $4s$ correspond to the two-photon resonance in both states, whereas the Ω in the first row correspond to the 16-photon and the 32-photon resonances, respectively.

Similar to the momentum maps in Fig. 4, these distributions are also plotted in logarithmic scale with contours decreasing in factors of e. Along with the photoabsorption rings, we also label the classical $2U_p$ limits in Fig. 5. The values of the $2U_p$ are the same for all values of Ω for a given initial state because varying the scaled frequency while retaining γ keeps the ponderomotive potential $U_p \propto F/\omega$ unchanged. For the lowest Ω values in the top two rows of Fig. 5, tunneling is the controlling mechanism for ionization as suggested by the low-momentum distributions, which are elongated in the laser polarization direction with a spread filling the $2U_p$ semicircles for both initial states. Also note that the minimum number of photons required for photoionization in these cases provides momenta substantially below that which would be provided by the $2U_p$ energy change induced by the classical laser field. Around $\Omega_1/\Omega \sim 2$, the spread at low momenta elongated in the $p_{||}$ direction for low Ω coalesces into a more spherically symmetric distribution around $p = 0$ a.u., and the photoabsorption rings are now more comparable in size with the $2U_p$ semicircles. Although $\Omega_1/\Omega \sim 2$ corresponds to frequencies which are a factor of two below the single-photon ionization limit for both initial states in Fig. 5, the continuous tunneling distributions at low momenta start separating into multiphoton absorption rings. These rings appear despite the fact that the frequency is below the single-photon absorption resonance due to the energy spread of the laser pulse. When the scaled frequency surpasses the Ω_1 limit, multiphoton ionization clearly takes over and the momentum distributions display multiphoton ionization rings at high scaled frequencies with $\Omega_1/\Omega = 0.5$ and 0.25 in Fig. 5. For $\Omega_1/\Omega = 2$ and below, ionization takes place through absorption of photons in the region $\Omega > \Omega_1$ for each initial state, even though $\gamma < 1$. The crossover between the tunneling and the multiphoton regimes is also evident from the time-dependent ionization probabilities in Fig. 6, which are for the lowest Ω in the top row of Fig. 5 and $\Omega_1/\Omega = 0.5$. For the low scaled frequencies

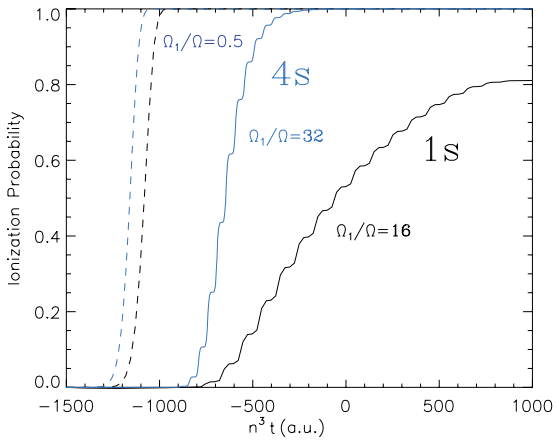

FIG. 6. (Color online) Time-dependent ionization probabilities for $\Omega_1/\Omega = 0.5$ and 16 from the initial state of $1s$ (black curves), and $\Omega_1/\Omega = 0.5$ and 32 from $4s$ (blue curves). While the high-Ω curves show no structure, the low-frequency curves display stepwise increase of the ionization probability, with the period matching the period of the driving laser. The laser pulse for $n = 1$ runs from -1600 to 1600 a.u., and the time axis is scaled by the factor n^3 to display the $4s$ curves inside the same time scale as the curves for $1s$.

(or high Ω_1/Ω) in Fig. 6, the black and blue solid curves show ionization in stepwise jumps with twice the frequency of the driving laser. This is a distinct signature of tunneling since ionization happens only at the peaks of the laser field. In the opposite case with the high Ω (or low Ω_1/Ω), ionization happens continuously and there is no structure in the ionization probabilities directly bearing information about either the laser field or the atomic motion.

The usual Keldysh parameter argument stating that $\gamma < 1$ corresponds to tunneling does not apply in the high-Ω region of the (γ,Ω) space, and it is true only when we use a factor of 2 or more below the single-photon ionization threshold in Ω. Tunneling prevails when the time scales associated with the electronic motion are much faster than the time scale set by the laser period and $\gamma < 1$. Another way to say this is that tunneling takes over when $\gamma < 1$ and the energy gained from the lowest-order multiphoton transition leading to continuum is much smaller than the classical $2U_p$ limit. In the opposite limit where the laser period is much shorter than the electronic time scales inside the atom, photoionization takes over even though $\gamma < 1$. The converse does not appear to be true, however; i.e., in the large-γ regime, the crossover between the atomic time scale and the laser period does not result in a crossover between the tunneling and the multiphoton ionization regimes, and multiphoton ionization always prevails in the $\gamma > 1$ regime.

V. SUMMARY

In conclusion, we have presented photoionization rates and probabilities out of the $1s$, $4s$, $8s$, and $16s$ states of the hydrogen atom for wide ranges of the Keldysh parameter γ and the scaled frequency Ω. We map the ionization rates using a cw laser and the probabilities using a laser pulse in (γ,Ω) space. By taking constant field strength and constant frequency slices from the (γ,Ω) maps, well-known hallmarks and structures for ionization rates can be reconstructed from both the common strong-field standpoint (Γ versus F) and the spectroscopic standpoint (Γ versus Ω) [2,6]. High-frequency suppression of ionization can also be seen beyond the single-photon ionization limit $\Omega_1 = n/2$ in both the ionization rates and the ionization probabilities in (γ,Ω) space, which was reported in Refs. [12,13].

We investigated momentum distributions of the ejected electrons at several points in the (γ,Ω) space in order to distinguish between tunnel ionization and photoionization for various ranges of γ and Ω. For the points we investigated in the large-γ region, the momentum distributions only show photoabsorption rings regardless of what the scaled frequency is, which is in agreement with the argument behind the Keldysh parameter that $\gamma > 1$ corresponds to multiphoton ionization. On the other hand, whether the multiphoton or the tunnel ionization dominates depends on the scaled frequency in the $\gamma < 1$ region. Although the Keldysh parameter argument predicts a tunneling picture for ionization when $\gamma < 1$, tunneling only prevails when Ω is also small compared to the single-photon ionization frequency $\Omega_1 = n/2$. Even though $\gamma < 1$, ionization takes place through photoabsorption in the region beyond Ω_1 for each initial state. Depending on the spectral width of the laser pulse, photoabsorption rings can

still be seen in the momentum distributions of the ejected electrons, even when the scaled frequency gets a factor of 2 below Ω_1. The tunneling can be though of as the limit when the atomic time scales are much shorter than the time scale set by the laser field only when $\gamma < 1$. Alternatively, this can also be expressed by saying that the tunneling prevails when the momentum, which the electron gains by absorbing the minimum necessary number of photons to escape, is small compared to the momentum to be gained from the ponderomotive motion in the laser field.

Pairing the Keldysh parameter with the scaled frequency serves to complement γ for its inadequacy to account for the relevance of the time scale inherently present in the bound electron dynamics, i.e., the classical period of the electron, as Keldysh-like theories assume no dynamics for the electron inside the potential well prior to ionization. The dynamical characterization outlined by γ is augmented by inclusion of the scaled frequency in this picture because the tunneling-multiphoton dichotomy suggested by the Keldysh parameter does not observe conservation of energy since it comes about within a strictly tunneling scenario. Both dynamical regimes of ionization may be attained for a chosen value of $\gamma < 1$ by varying the scaled frequency.

ACKNOWLEDGMENTS

This work was supported by the Office of Basic Energy Sciences, US Department of Energy. Computational work was carried out at the National Energy Research Scientific Computing (NERSC) Center in Oakland, California.

[1] V. S. Popov, Phys. Usp. **47**, 855 (2004).
[2] N. B. Delone and V. P. Krainov, Phys. Usp. **41**, 469 (1998).
[3] H. R. Reiss, Prog. Quantum Electron. **16**, 1 (1992).
[4] P. W. Milonni, Phys. Rev. A **38**, 2682 (1988).
[5] F. Trombetta, S. Basile, and G. Ferrante, Phys. Rev. A **40**, 2774 (1989).
[6] M. Dörr, R. M. Potvliege, D. Proulx, and R. Shakeshaft, Phys. Rev. A **42**, 4138 (1990).
[7] H. R. Reiss, Phys. Rev. A **82**, 023418 (2010).
[8] M. V. Frolov, A. V. Flegel, N. L. Manakov, and A. F. Starace, J. Phys. B **38**, L375 (2005).
[9] Y. Ni, S. Zamith, F. Lepine, T. Martchenko, M. Kling, O. Ghafur, H. G. Muller, G. Berden, F. Robicheaux, and M. J. J. Vrakking, Phys. Rev. A **78**, 013413 (2008).
[10] J. H. Gurian, K. R. Overstreet, H. Maeda, and T. F. Gallagher, Phys. Rev. A **82**, 043415 (2010).
[11] T. Topcu and F. Robicheaux, J. Phys. B **40**, 1925 (2007).
[12] E. J. Galvez, B. E. Sauer, L. Moorman, P. M. Koch, and D. Richards, Phys. Rev. Lett. **61**, 2011 (1988).
[13] H. Maeda and T. F. Gallagher, Phys. Rev. Lett. **93**, 193002 (2004).
[14] P. B. Corkum, N. H. Burnett, and F. Brunel, Phys. Rev. Lett. **62**, 1259 (1989).
[15] B. Walker, B. Sheehy, K. C. Kulander, and L. F. DiMauro, Phys. Rev. Lett. **77**, 5031 (1996).
[16] Z. Chen, T. Morishita, A.-T. Le, and C. D. Lin, Phys. Rev. A **76**, 043402 (2007).